Proton-Irradiated Tin Oxyhydroxide Nanoparticle Anodes for Enhanced Lithium-Ion Storage

Jaewoo Lee, Seunguk Cheon, Sung Oh Cho*
Dept. of Nucelar & Quantum Engineering, Korea Advanced Institute of Science & Technology, Daejeon, Republic of Korea, 34141
**Corresponding author: socho@kaist.ac.kr*

1. Introduction

Ion irradiation is one of the most efficient routes to altering various properties of materials with the help of energetic charged particles. The primary effects are electronic and structural transformation, which originates from the displacement of constituent atoms. Particularly, materials are subject to be defective during ion irradiation, and such defective nature further leads to the amorphization of materials. Many papers have reported that ion irradiation induces defect generation and amorphization in materials [1,2].

Compared with other methods, ion irradiation can achieve a high density of defects and selective defect types. In addition, it can be employed at room temperature for a relatively short time. Therefore, drastic changes in material properties are easily accomplished by irradiating ions into materials.

Meanwhile, defective and amorphous materials have been widely applied in various electrochemical fields [3,4], and the most promising application is anode materials for lithium-ion batteries. When the anode materials involve some defect sites, the electrochemical properties can be enhanced [5]. Furthermore, the amorphous phase of anode materials also improves the reaction kinetics [6].

In this study, we investigated the effects of ion irradiation on tin oxyhydroxide nanoparticle anodes, which are potential candidates for lithium-ion batteries. Proton was chosen as irradiating ion type to evolve defects and phase transformation in the anodes. The proton-irradiated anodes were also evaluated in terms of battery performance. Ion irradiation is highly applicable to not only battery anodes but diverse electrochemical purposes.

2. Experimental Section

2.1 Electrode Preparation

Tin oxyhydroxide ($Sn_6O_4(OH)_4$) nanoparticles were directly obtained using the electrochemical anodization method and served as anode active materials. To fabricate electrodes, the nanoparticles were mixed with conducting agent (Super P, Imerys, France) and binder (polyvinylidene fluoride, PVDF) in N-methyl-2-pyrrolidone solvent at a weight ratio of 4:5:1. The resulting slurry was cast on copper foil with 10 μm thickness at a loading level of about 0.5 mg cm^{-2}. The prepared electrodes were 30% roll-pressed at 75℃ and were dried in a vacuum at 80℃ for 12 hr.

2.2 Ion Irradiation

Prior to irradiating protons into the electrode, simulation was carried out using the Stopping Range of Ions in Matter (SRIM-2013) code developed by James F. Ziegler. H ions were selected as incident ions with the angle of incidence of 0, and “Ion Distribution and Quick Calculation of Damage” and “Ion Distribution with Recoils projected on Y-Plane” were chosen for the damage type and basic plots respectively. For a target layer, H, O, and Sn, which are components of $Sn_6O_4(OH)_4$, were assigned with an atomic ratio of 4:8:6. C was allocated for conducting agent, and H, C, and F were also assigned equally for PVDF. Overall atomic stoichiometry was properly input according to the mixing ratio of 4:5:1. The displacement damage of H, C, O, F, and Sn was set to 10, 28, 28, 25, and 25 eV, respectively. The layer width was 10 μm and density was 0.5 g cm^{-3} by the loading level. The total number of ions was 10000 for approximate distribution. For outputs, “Ion Ranges”, “Backscattered Ions”, and “Transmitted Ions/Recoils” were selected.

Proton irradiation was operated by an ion implanter (0.4 MV, Korea Institute of Science and Technology, Korea) with multi-energy of 15, 100, and 180 keV. The exposed area was 3.2 cm × 3.2 cm and the current was 40 μA. Proton fluence was chosen to be 1×10^{15}, 1×10^{16}, and 1×10^{17} cm^{-2}. The irradiation was performed in the air at room temperature.

2.3 Characterization

The surface condition of electrodes before and after proton irradiation was characterized using a field-emission scanning electron microscope (FESEM, Magellan400, FEI Company, USA). The elemental investigation was carried out with an energy-dispersive X-ray spectrometer (EDS) involved in FESEM. Chemical analysis was conducted using a high-resolution Raman/PL system (LabRAM HR Evolution Visible_NIR, HORIBA, Japan) with a 514 nm laser, an electron spin resonance spectrometer (ESR, JES-FA100, JEOL, Japan) in a vacuum at room temperature, a Fourier-transform infrared spectrometer (FT-IR, Nicolet iS50, Thermo Fisher Scientific Instrument, USA), and an X-ray photoelectron spectrometer (XPS, K-alpha,

Thermo VG Scientific, USA) with Al Kα radiation (1486.7 eV).

2.4 Electrochemical Measurement

CR2032-type coin cells were assembled with the prepared electrodes as anodes (working electrodes with a diameter of 15 mm) and lithium foil (16 mm in diameter and 300 μm in thickness) as counter electrodes. A 16 μm thickness of polyethylene separator (19 mm in diameter) was placed between the working and counter electrodes. 1 mol L^{-1} lithium hexafluorophosphate dissolved in a mixed solvent with ethylene carbonate, dimethyl carbonate, and ethyl methyl carbonate (1:1:1 v/v) including 3 wt% fluoroethylene carbonate additive was used as an electrolyte solution. A galvanostatic charging-discharging cycling test of the coin cells was performed in a potential range between 0.005 and 3 V (vs. Li/Li^+) at room temperature using a cell cycle tester (WBCS3000Le32, WonATech, Korea).

3. Results and Discussion

The thickness of tin oxyhydroxide nanoparticle electrodes was measured to be 20 μm as shown in Fig. 1a. Since the thickness of the copper substrate is 10 μm, the electrode material, which is the target layer, is 10 μm in thickness. The average proton range in the electrode material depending on proton energy is shown in Fig. 1b. It is clearly seen that the ranges corresponding to each irradiating energy (15, 100, and 180 keV) are lower than 10 μm. Each energy can be allocated to surface, central, and deep irradiation, respectively. Fig 2a-c give the simulated damage distribution of electrode material with three-energy irradiation depending on proton fluence. The amount of damage can be expressed in displacement per atom (dpa), which is calculated by Eq. 1 [7].

$$dpa = \frac{The\ number\ of\ total\ vacancies}{Atom\ density} \times Ion\ fluence \quad (1)$$

where the number of total vacancies is the sum of the number of vacancies induced by ions and recoils in the unit of cm^{-1} and atom density is the number of atoms present in a unit volume of a matter in the unit of cm^{-3}. Therefore, dpa has no units. There are Bragg peaks in the dpa distribution for all fluence conditions and peak positions are 0.8, 4.1, and 7.3 μm. The maximum dpa is approximately 0.004, 0.04, and 0.4 for a fluence of 1×10^{15}, 1×10^{16}, and 1×10^{17} cm^{-2}, respectively.

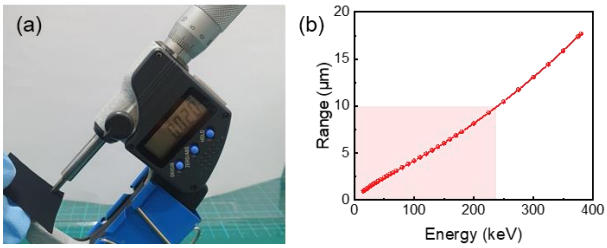

Fig. 1. (a) Digital photograph of measuring tin oxyhydroxide nanoparticle electrode thickness. (b) Calculated proton range in the electrode material depending on proton energy.

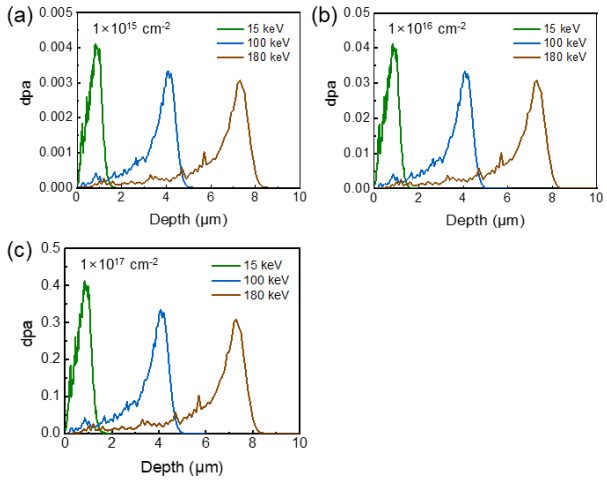

Fig. 2. Calculated dpa distribution of tin oxyhydroxide nanoparticle electrode irradiated with protons at a fluence of (a) 1×10^{15}, (b) 1×10^{16}, and (c) 1×10^{17} cm^{-2}.

Fig. 3a shows the surface of the tin oxyhydroxide nanoparticle electrode before proton irradiation. Although dpa profiles have sharp Bragg peaks, actual damage would be spread broadly due to the highly porous structure of the electrode surface. After considerable proton irradiation, there are no remarkable changes in the surface as shown in Fig. 3b-d. Nevertheless, EDS results in Table I suggest that the electrode has no fluorine component after irradiation with protons at a fluence of 1×10^{17} cm^{-2}. Since fluorine is present only in PVDF, it implies that PVDF may be damaged due to high-fluence proton irradiation. Conversely, oxygen content becomes larger after irradiation, supporting air oxidation of the electrode surface during irradiation, which is a common feature of ion irradiation.

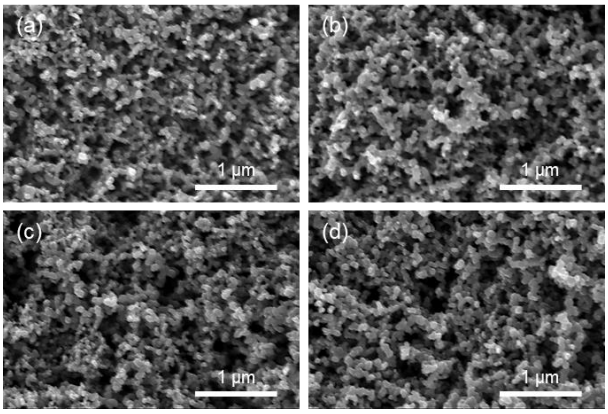

Fig. 3. FESEM images of the surface of tin oxyhydroxide nanoparticle electrode (a) before proton irradiation and irradiated with protons at a fluence of (b) 1×10^{15}, (c) 1×10^{16}, and (d) 1×10^{17} cm^{-2}.

Table I: Elemental content of the surface of tin oxyhydroxide nanoparticle electrode before and after proton irradiation at a fluence of 1×10^{17} cm^{-2}.

Electrode	Before irradiation	After irradiation
C (wt%)	89.14	83.72
O (wt%)	1.72	3.41
F (wt%)	1.74	0
Sn (wt%)	7.40	12.87

Further chemical investigations were conducted, and Fig. 4a shows Raman spectra of tin oxyhydroxide nanoparticle electrodes before and after proton irradiation. There are two distinct peaks in the case of the pristine electrode, where the peaks correspond to the D band (1358 cm^{-1}) and G band (1604 cm^{-1}) of carbon (conducting agent). The peaks are wider as proton fluence increases, resulting in the amorphization of carbon. The lower G peak position is observed at the higher fluence and the intensity ratio between the D peak and G peak (I_D/I_G) is reduced after high-fluence irradiation. It has been accepted that the lower G peak position and I_D/I_G in carbon materials are induced by changes in energy level due to defect creation, where aromatic bonds are broken by proton irradiation [8]. It also leads to creating C· radicals in the electrode surface. Fig. 4b shows the ESR spectra of the electrodes depending on proton fluence. All of the electrodes have a signal near a magnetic field of 330 mT, which corresponds to g = 1.995. g can be calculated by the microwave frequency and the magnetic field used in the measurement. The signal at g = 1.995 is ascribed to surface defect and oxygen vacancy (VO) in materials and it is clearly seen that the intensity of the signal significantly grows when the proton fluence is high. Accordingly, a large number of defects are generated in the tin oxyhydroxide nanoparticle anode after proton irradiation.

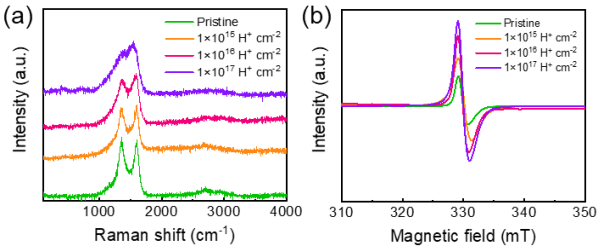

Fig. 4. (a) Raman and (b) ESR spectra of tin oxyhydroxide nanoparticle electrode before and after proton irradiation.

To identify the damage to the electrode materials, FT-IR spectra are given in Fig. 5. General behavior of transmittance is similar for all electrodes, but no peaks are found for the irradiated electrodes in the enlarged spectra. Each peak is assigned to (1) $–CH_2$ and $–CF_2$, (2) α-PVDF, and (3) β-PVDF for 1390, 1160, and 870 cm^{-1}, respectively. The absent PVDF-related peaks after proton irradiation support the amorphization of the binder. Fig. 6a-c show the XPS spectra of the electrode before and after irradiation. All peaks were deconvolved by referring to C 1s peak (284.8 eV). The VO peak at 531.5 eV in Fig. 6a gets larger as fluence increases due to the breaking of weak O-O bonds. The VO creation after proton irradiation is in line with the ESR results and the smoother profile suggests more oxygen content at the electrode surface from surface oxidation during irradiation. In Fig. 6b, existing sp^2 C-C bonds (284.8 eV) are considerably converted into sp^3 C-C bonds (285.6 eV) at higher fluence. It results from the breaking of aromatic rings, which accompanies a decrease in I_D/I_G. Additionally, fewer C-F_2 groups (291.0 eV) are observed at higher fluence due to the decomposition of PVDF. The damage on PVDF can be also confirmed in Fig. 6c. The C-F_2 peak (688.0 eV) becomes smaller after high-fluence irradiation, and simultaneously, C-F bonds (687.1 eV) arise due to the removal of F. Unclear profile at higher fluence also implies the less content of fluorine.

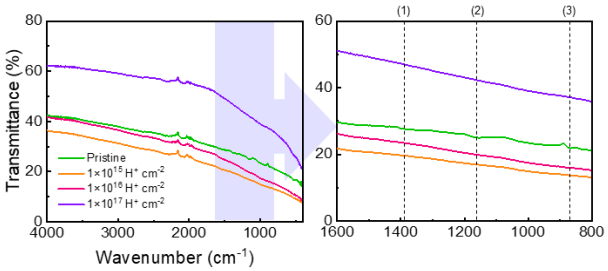

Fig. 5. FT-IR spectra of tin oxyhydroxide nanoparticle electrode before and after proton irradiation.

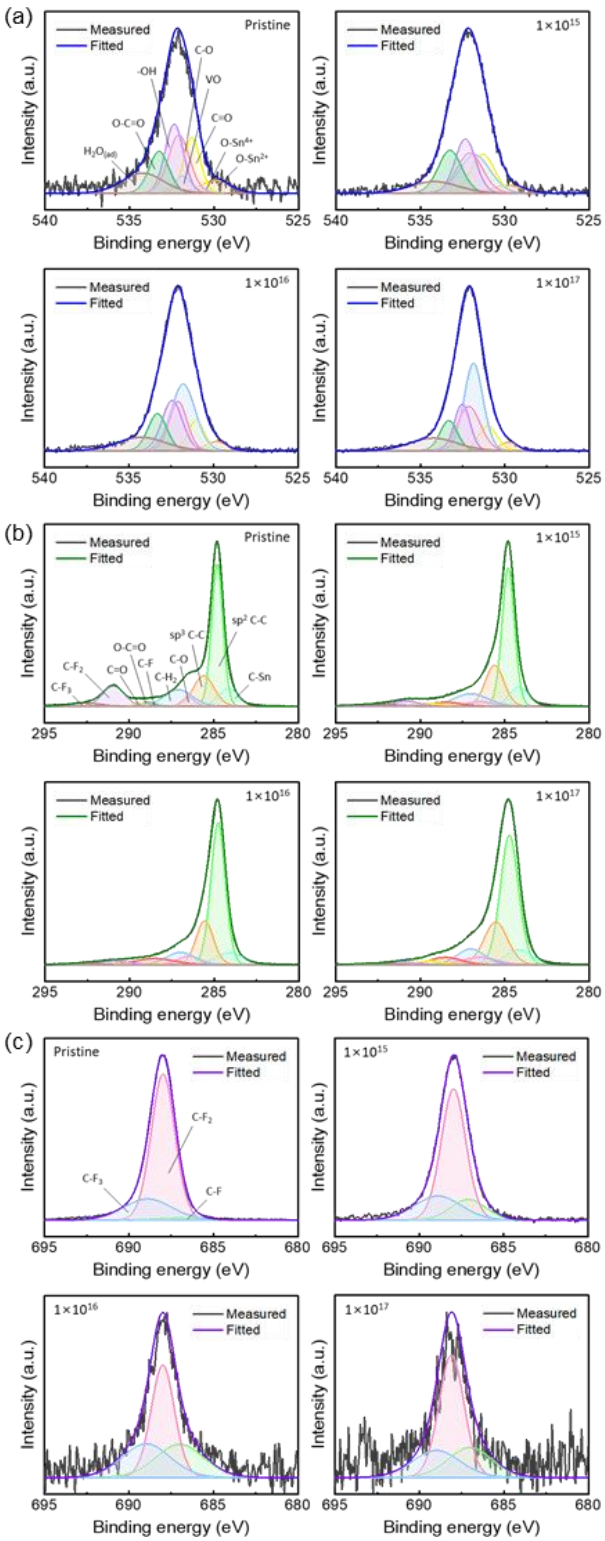

Fig. 6. (a) O 1s, (b) C 1s, and (c) F 1s XPS spectra of tin oxyhydroxide nanoparticle electrode before and after proton irradiation.

Subsequently, the electrochemical performance of the proton-irradiated electrodes was evaluated, and Fig. 7 presents the cycle characteristic of the electrodes before and after proton irradiation. The first cycle was performed at a low current rate of 0.1 C (1 C: 838.05 mA g^{-1}) to activate the reaction sites and the remaining cycles were performed at 0.5 C. The low-fluence-irradiated (1×10^{15} cm^{-2}) and middle-fluence-irradiated (1×10^{16} cm^{-2}) electrodes exhibit similar discharge capacity to that of the pristine electrode, but slightly higher as fluence increases. Initial coulombic efficiency is approximately 65.6%, 61.0%, and 63.3% for pristine, low-fluence, and high-fluence electrodes, respectively. However, when a high fluence of protons (1×10^{17} cm^{-2}) is irradiated into the tin oxyhydroxide nanoparticle anode, a much larger capacity is achieved. It may result from the presence of rich defects in the electrode surface, which serve additional electrochemical reaction sites [6]. Moreover, the higher initial coulombic efficiency of 70.8% for the highly irradiated electrode is ascribed to less irreversible solid-electrolyte interface (SEI) formation. A lot of C· radicals created by proton irradiation combine with tin oxyhydroxide, creating Sn-C or Sn-O-C bonds, and the carbon regions prevent the SEI formation. As a result, high-fluence proton irradiation to tin oxyhydroxide nanoparticle anode leads to an increase in capacity and improves the initial coulombic efficiency, enhancing the electrochemical properties.

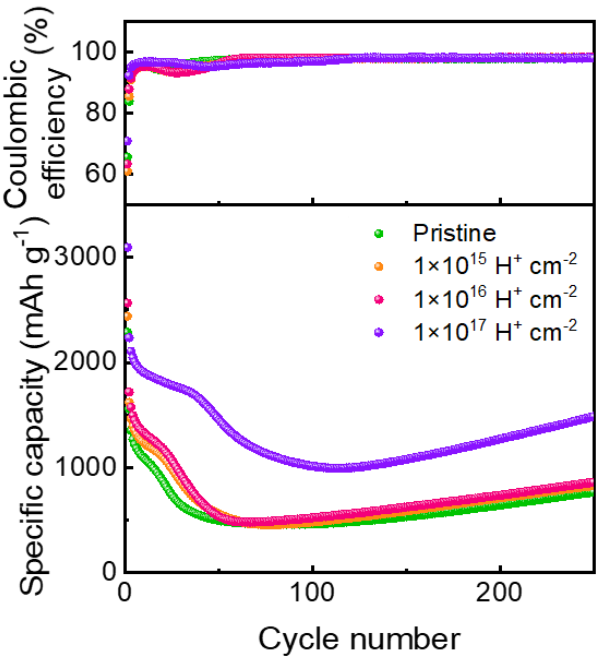

Fig. 7. Electrochemical cycle performance at a current rate of 0.5 C of tin oxyhydroxide nanoparticle electrode before and after proton irradiation.

4. Conclusions

Proton irradiation effects on structural and electrochemical properties of tin oxyhydroxide nanoparticle electrodes for lithium-ion battery anodes were investigated. Plentiful defects and radicals were introduced in the carbonaceous conducting agent of electrode materials after proton irradiation, resulting in

the amorphization of carbon. The defects and radicals played a key role to improve the electrochemical performance of tin oxyhydroxide nanoparticle anodes. The proton irradiation also led to VO generation and damaged PVDF, which also allowed enhanced electrochemical properties. Ion irradiation as well as protons can be applied to miscellaneous electrochemical fields by efficiently altering the material properties.

ACKNOWLEDGEMENTS

This work was supported by the National Research Foundation of Korea (NRF) grant funded by the Korean government (MSIT) (No. 2022M2E9A3048435 and No. 2019M2D2A1A02058174).

REFERENCES

[1] X. Xiang, Z. He, J. Rao, Z. Fan, X. Wang, and Y. Chen, Applications of Ion Beam Irradiation in Multifunctional Oxide Thin Films: A Review, ACS Applied Electronic Materials, Vol.3, pp.1031-1042, 2021.
[2] G. Pilania, K.R. Whittle, C. Jiang, R.W. Grimes, C.R. Stanek, K.E. Sickafus, and B.P. Uberuaga, Using Machine Learning To Identify Factors That Govern Amorphization of Irradiated Pyrochlores, Chemistry of Materials, Vol.29, pp.2574-2583, 2017.
[3] C. Meng, M. Lin, X. Sun, X. Chen, X. Chen, X. Du, and Y. Zhou, Laser Synthesis of Oxygen Vacancy-Modified CoOOH for Highly Efficient Oxygen Evolution, Chemical Communications, Vol.55, pp.2904-2907, 2019.
[4] B. Kim, M.K. Kabiraz, J. Lee, C. Choi, H. Baik, Y. Jung, H.-S. Oh, S.-I. Choi, and K. Lee, Vertical-Crystalline Fe-Doped β-Ni Oxyhydroxides for Highly Active and Stable Oxygen Evolution Reaction, Matter, Vol.4, pp.3585-3604, 2021.
[5] M.M. Rahman, W.-Y. Chen, L. Mu, Z. Xu, Z. Xiao, M. Li, X.-M. Bai, and F. Lin, Defect and structural evolution under high-energy ion irradiation informs battery materials design for extreme environments, Nature Communications, Vol.11, p.4548, 2020.
[6] S. Yan, K.P. Abhilash, L. Tang, M. Yang, Y. Ma, Q. Xia, Q. Guo, and H. Xia, Research Advances of Amorphous Metal Oxides in Electrochemical Energy Storage and Conversion, Small, Vol.15, p.1804371, 2019.
[7] J.F. Ziegler and J.P. Biersack, The Stopping and Range of Ions in Matter, In: D.A. Bromley (eds), Treatise on Heavy-Ion Science, Springer, Boston, MA, 1985.
[8] J. Robertson, Diamond-like amorphous carbon, Materials Science and Engineering: R: Reports, Vol.37, pp.129-281, 2002.